CHINESE OPTICS LETTERS

Vol. 21, No. 7 | July 2023

Active tuning of Si metasurface with large area

Bintao Du (杜滨涛), Zhihai Wu (吴之海), Chengkun Dong (董成坤), Jun Wu (吴 俊), and Jun Xia (夏 军)*

Joint International Research Laboratory of Information Display and Visualization, School of Electronic Science and Engineering, Southeast University, Nanjing 210096, China

*Corresponding author: xiajun@seu.edu.cn

Received February 18, 2023 | Accepted April 14, 2023 | Posted Online July 12, 2023

All-dielectric metasurfaces are usually limited because of their static functionality and small scale. In this paper, we use an easy nanofabrication technique to fabricate all-dielectric metasurfaces with the advantages of having dynamic tunability and a large area. Using an anodized aluminum oxide (AAO) template as an evaporation mask, a large-area metasurface embedded in polydimethylsiloxane (PDMS) ($>2\ \mathrm{cm}^2$) is fabricated. The metasurface exhibits remarkable electric dipole (ED) and magnetic dipole (MD) resonances. Based on the solvent-swelling effect of PDMS in 20% toluene, the ED/MD resonance peak shifts dynamically ~40 nm to red. So far, to the best of our knowledge, a large-area metasurface embedded in PDMS and achieved by using the AAO template method has not appeared.

Keywords: all-dielectric metasurface; light manipulation; nanodisk; dynamic tunability.
DOI: 10.3788/COL202321.073601

1. Introduction

Recently, all-dielectric metasurfaces have received extensive attention due to their promising potential in compact optical devices[1–7], originating from manipulating the amplitude[8–10], phase[11,12], and polarization of light[13,14] with a high efficiency. Different from the plasmonic metasurfaces, all-dielectric metasurfaces exhibit Mie-type resonances without strong ohmic losses[8,9]. However, most presented metasurfaces are based on static designs, and their functionality cannot be changed once the structures are fabricated[15–17]. In some applications, it is important to enable the dynamic tunability of metasurface functionality with time[18–26]. Moreover, all-dielectric metasurfaces are usually limited to a small scale, which are fabricated by electron beam lithography (EBL) and focused ion beam (FIB) lithography[27].

In this work, we describe an easy approach with advantages of dynamic tunability and large area in which a large-area Si metasurface embedded in polydimethylsiloxane (PDMS) is fabricated by combining the anodized aluminum oxide (AAO) template method with a sacrificial layer dissolution. Using an AAO template as an evaporation mask, Si vapor is deposited through the AAO template onto an Al sacrificial layer. After complete dissolution of the sacrificial layer, a Si nanocylinder array embedded in the PDMS is fabricated. Furthermore, with the metasurface immersed in 20% toluene, the electric dipole (ED) and magnetic dipole (MD) resonances both undergo a dynamic red shift around 40 nm. Compared with the metasurfaces produced by EBL and FIB, our approach can realize a dynamic metasurface with a large area in an easier way. Additionally, in this paper, the large-area metasurface embedded in the PDMS would offer great ease for applications in curved surface devices, such as LEDs, wearable electronics, or other optoelectronic devices.

2. Method

In the following section, we introduce the fabrication of a dynamic metasurface with a large area. Figures 1(a)–1(i) display the stepwise process of fabrication.

The AAO template with polymethyl methacrylate (PMMA) supported in this paper is purchased from WUXI YIRI Advanced Materials Technology Co., Ltd., as illustrated in Fig. 1(a). The hole diameter and mean interhole distance of the AAO template are around 300 nm and 450 nm, respectively. The AAO template is usually fabricated by multistep anodization and wet etching under a proper direct current voltage[28,29]. The hole diameter and interhole distance of the AAO template can be controlled by varying the applied voltage and oxidation time.

Next, acetone is used to dissolve the layer of PMMA, as shown in Fig. 1(b). With the PMMA completely dissolved, the bare AAO template is transferred to a new substrate, which is deposited on a 200-nm Al sacrificial layer beforehand. Note that Al is easily oxidized to aluminum trioxide in the air. Therefore, the new substrate used in Fig. 1(c) is coated with Al and Al_2O_3 layers. After natural drying the AAO template in a clean room, the Si vapor is deposited into the holes of AAO using electron beam evaporation, as shown in Fig. 1(d). After depositing the

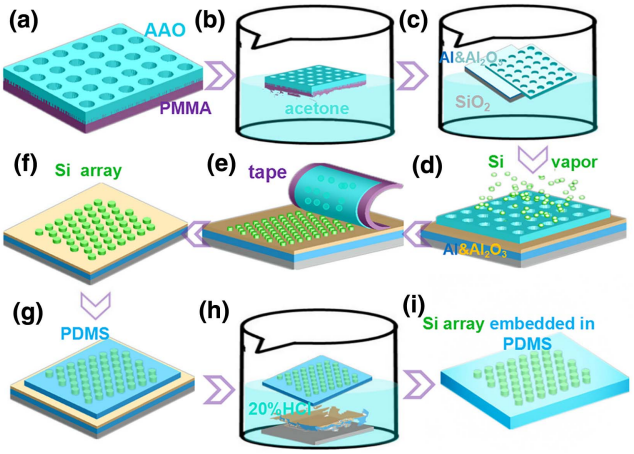

Fig. 1. Fabrication steps of the dynamic metasurface with a large area. (a) The AAO template with PMMA support. (b) The dissolution of the PMMA using acetone. (c) The transfer of the AAO by a new substrate. (d) The Si deposition using electron beam evaporation. (e) The detachment of the AAO with adhesive tape. (f) The Si metasurface with a large area. (g) The PDMS coating and curing. (h) The sacrificial layer dissolution in 20% HCl. (i) The Si metasurface embedded in the PDMS.

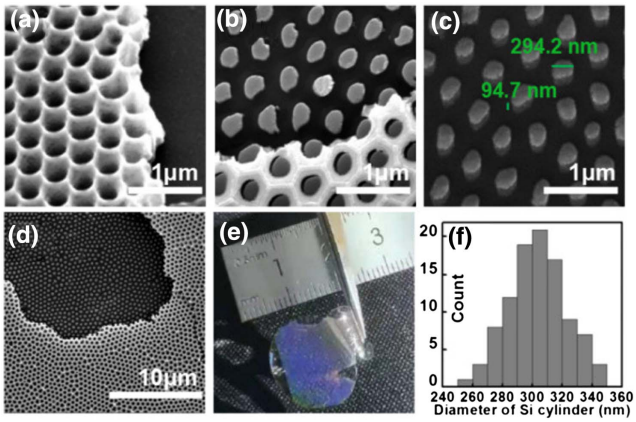

Fig. 2. (a) The SEM image of the AAO template with a 45° tilt view. (b) The SEM image of the Si metasurface with the top view. (c) The SEM image of the Si metasurface with a 45° tilt view. (d) The SEM image of the Si metasurface with a large area. (e) The photograph of the metasurface embedded in the PDMS. (f) The histogram of the diameter distribution.

100-nm Si, adhesive tape is used to peel off the AAO and excess Si from the substrate. The array of Si nanocylinders is formed over a large area on the substrate, as shown in Fig. 1(f). In Fig. 1(g), a mixture of PDMS pre-polymer (Sylgard 184, Dow Corning) and its curing agent is spin coated over the top of the Si metasurface, followed by curing at 60°C for 4 hours. Afterwards, the sample is immersed in 20% HCl to dissolve the sacrificial layer of Al and Al_2O_3. Twelve hours later, the Si metasurface embedded in the PDMS is detached from the substrate naturally, as shown in Fig. 1(h). It should be noted that the PDMS and Si nanocylinder do not react with HCl during the whole dissolution process, while the Al and Al_2O_3 do. Finally, deionized water is used to rinse the sample, and it is dried under a nitrogen flow, as shown in Fig. 1(i).

The softness and lightness of the AAO template lead to wrinkles easily. It is difficult to successfully transfer the AAO template at one time. It usually takes several times. Next, we introduce the details of the AAO template transfer corresponding to Fig. 1(c). As shown in Fig. 1(c), the substrate with the inclination angle is immersed into the acetone for transferring. One side of the substrate is used to poke a corner of the AAO template. As the substrate is lifted, the AAO template is raised up and attached to the substrate surface naturally. The AAO template is flat on the new substrate. If the substrate is immersed and lifted without the inclination angle, then the AAO would not be transferred successfully. As the acetone flows, the AAO template slips.

The scanning electron microscopy (SEM) image of the AAO template with a 45° tilt view is shown in Fig. 2(a). According to our statistics, the mean diameter and interhole distance of the transferred AAO template here are 309.4 nm and 458.1 nm, respectively, which are close to the initial parameters in Fig. 1(a). Figures 2(b) and 2(c) show the SEM images of the Si metasurface with a top-view and a 45° tilt view after the AAO template is detached. In the top view image, the template has been partially removed using adhesive tape to reveal the Si nanocylinders on the surface. In Fig. 2(c), the diameter and height of the nanocylinders are 294.2 nm and 94.7 nm, respectively. Another SEM of the Si metasurface with a large area is visible in Fig. 2(d). Figure 2(e) shows the photograph of the Si metasurface embedded in the PDMS, fabricated as described above, clearly demonstrating a square area of about 1.5 cm × 1.5 cm. Because the PDMS is not completely flat in the air, different inclination angles lead to different colors. The thickness of the PDMS here is about 156.6 μm, which is measured by a step profiler (AMBios Technology, XP-1). In fact, the thickness of the PDMS can be controlled by the spin speed and the duration time according to the need. We measure the diameter distribution of the Si cylinder, and a statistic histogram is shown in Fig. 2(f).

3. Result and Discussion

For optical characterization of the Si metasurface embedded in the PDMS, we measure the transmission spectra, as shown in Fig. 3(a). The transmitted light is collected and measured by an optical spectroscopic system (Ocean Optics Flame; 200–1100 nm) equipped with a white light source (Ocean Optics Tungsten Halogen Light Source). A fiber is used to guide the light, and a collimating lens (74-UV) is applied for collimating the light. They are connected by a fiber coupler. Between the collimating lenses, the PDMS with different stretching is fixed on a stage. The latter collimating lens behind the PDMS is applied to couple the light into the optical spectrometer.

First, the metasurface without any strain is measured with the optical spectrometer, as shown in Fig. 3(a). The red curve in Fig. 3(b) presents the measured result. Two clear dips are

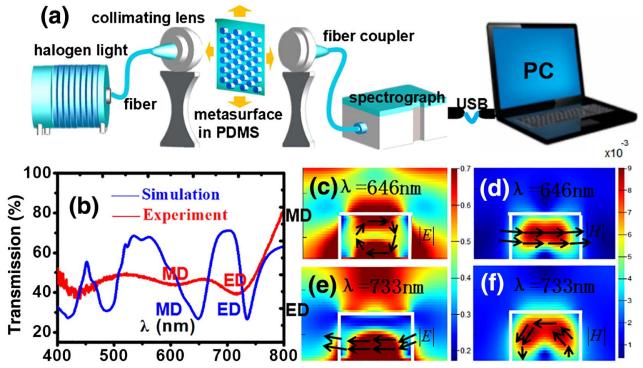

Fig. 3. (a) The schematic of the optical setup used to measure the metasurface. (b) The measured (red line) and simulated (blue line) transmission spectra of the Si metasurface embedded in the PDMS without any strain. (c) The electric field of the MD at λ = 646 nm. (d) The magnetic field of the MD at λ = 646 nm. (e) The electric field of the ED at λ = 733 nm. (f) The magnetic field of the ED at λ = 733 nm. The direction of the field is shown by arrows, and the strength of the field is indicated by the color.

observed, which correspond to the ED mode at $\lambda = 716$ nm and the MD resonance at $\lambda = 612$ nm. To verify the experimental results, finite-difference time-domain (FDTD) simulation is carried out with the Si metasurface in the relaxed mode. In simulation [blue curve in Fig. 3(b)], the resonant position at $\lambda = 733$ nm is the ED, whereas the resonant position at $\lambda = 646$ nm corresponds to the MD. As discussed above, with the AAO (300 nm diameter and 450 nm interhole) as a template, the ED/MD resonance easily appears at a visible spectrum. This may have great potential application in solar cells, organic light-emitting diodes, and photoluminescence (PL) enhancement. However, the resonances of the ED and the MD modes in experiment are less dramatic than those in the simulation. Such a moderate efficiency may be attributed to several reasons. First, the simulation assumes that the Si cylinders have ideal shapes, but the fabricated cylinders exhibit irregularities. Second, the array defect and PDMS thickness would also contribute. In order to improve the optical properties of the ED/MD resonance, it is better to create a perfect template by nanoimprint technology. The nanoimprint technique can fabricate the template with perfect topography. Moreover, atomic layer deposition (ALD) can be employed to deposit Si vapor, which produces smoother deposition on the template. Additionally, the Si cylinder array can be optimized by chemical etching, as shown in Fig. 1(h), resulting in a complete removal of the AAO template. This avoids the Si array defect by tape detachment. The other dips before 500 nm originate from the excitation of a higher-order mode or grating effect, which are not considered in this paper. In the following, we will concentrate on the discussion of the ED and the MD modes.

To gain more insight into the characteristics of the resonance, the electromagnetic near-field distributions around the nanocylinders are simulated in Figs. 3(c)–3(f). For resonance at $\lambda = 646$ nm, as shown in Figs. 3(c) and 3(d), the electric field is highly confined to the top and bottom and even the lateral surfaces of the nanocylinder. The electric field inside the nanocylinder at this resonance has a circular displacement, while the magnetic field oscillates in the nanocylinder center, clearly indicating the formation of the magnetic dipole resonance[30]. For the resonance at $\lambda = 733$ nm, the enhanced electric field and vortex-like magnetic field demonstrate the excitation of an electric dipole resonance[30], as shown in Figs. 3(e) and 3(f). Due to the interaction with the substrate, the circular distribution of the magnetic field is distorted in Fig. 3(f). As discussed above, it is easy to see that the resonance at $\lambda = 733$ nm is the ED mode, whereas the resonance at $\lambda = 646$ nm is the well-known MD mode.

The metasurface tunability in this paper is achieved by changing the unit cell period. Figure 4(a) presents the Si metasurface embedded in the PDMS in the relaxed mode. To induce change of the metasurface period, the fabricated metasurface is immersed in toluene with different concentrations for 20 minutes, as shown in Fig. 4(b). Because the swelling magnitude of the PDMS film significantly depends on the polarity of solution, we can flexibly control the period of the Si metasurface by tuning the toluene concentration[31,32]. Twenty minutes later, deionized water is used to rinse the metasurface embedded in the PDMS, and it is quickly dried under a nitrogen flow. As the final step, the metasurface is measured with an optical spectrometer.

After the immersion in the toluene solution with 10% concentration, as visible in Fig. 4(c), the ED resonance shifts from 716 nm to 732 nm. Simultaneously, the MD resonance undergoes a red shift from 612 nm to 626 nm. As the toluene concentration increases from 10% to 20%, the ED resonance continuously shifts from 732 nm to 756 nm. Similarly, the MD resonance also shifts from 626 nm to 648 nm. The green dashed lines in Fig. 4(c) trace the ED/MD resonant dip position, and apparently, it red shifts for the measured spectra. In total, a

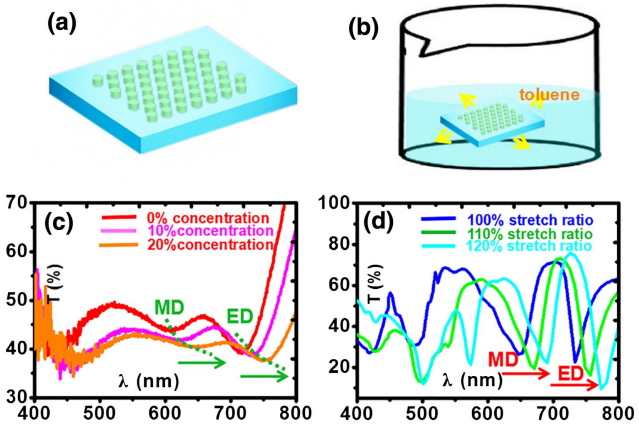

Fig. 4. (a) The sketch of the Si metasurface embedded in the PDMS. (b) The sketch of the metasurface immersed in toluene. (c) The measured transmittance of the metasurface after immersion in the toluene with different concentrations. Red, magenta, and orange correspond to concentrations of 0%, 10%, and 20%, respectively. (d) The simulated transmittance of the metasurface with the corresponding stretch ratio. Blue, green, and cyan correspond to the stretch ratios of 100%, 113%, and 122%, respectively.

20% concentration increase gives rise to 40-nm red shift for the ED resonance and 36 nm for the MD resonance. It should be noted that, as time goes by, the PDMS will shrink back to its original state, and the ED/MD also recovers their initial positions. In addition to the PDMS swelling, mechanical stretching is also a good choice for metasurface tunability.

The ED/MD resonance shifting can also be verified by simulation, as visible in Fig. 4(d). According to the PDMS swelling coefficient in toluene, 10% toluene results in a 113% stretch ratio[31,32], corresponding to a period increase to 508.5 nm (450% × 113%). As a result, the ED resonance shifts from 733 nm to 756 nm, and the corresponding MD resonance increases from 646 nm to 671 nm in simulation. Further increasing the toluene concentration to 20% toluene leads to a 122% stretch ratio[31,32], corresponding to a period increase to 549 nm (450% × 122%). Correspondingly, the ED resonance continuously shifts from 756 nm to 773 nm, whereas the MD resonance shifts from 671 nm to 690 nm. In total, a 40 nm and a 44 nm red shifts for the ED resonance and the MD resonance are observed as the toluene concentration increases to 20%. Overall, the trend of simulation is quite consistent with that of the experiment, with slight difference arising from fabrication tolerances and the PDMS thickness deviation. The two dips, labeled ED and MD, both show a clear red shift of about 40 nm, whether in simulation or experiment. There is a clear dip at 580 nm for the 122% stretch ratio in Fig. 4(d). In fact, there are another two dips located at 530 nm and 550 nm, corresponding to 100% and 113% stretch ratios, respectively. These dips in simulation may result from the electric quadrupole (EQ) or the magnetic quadrupole (MQ) resonance (higher-order mode)[33].

Note that the nanofabrication techniques using EBL or FIB cannot be directly applied to the arbitrarily cured surfaces now. As a flexible and stretchable elastic membrane, the PDMS containing the large-area metasurface can easily be attached to the arbitrarily curved substrates. Therefore, such flexible metasurfaces fabricated as described above can find applications in curved surface devices[34–37], such as LEDs, wearable electronics, or other optoelectronic devices. The dynamic system proposed in this paper may find potential applications in color writing and printing[38], sensors, and intelligent detectors.

4. Conclusion

In this paper, we use a new method to fabricate a large-area metasurface embedded in PDMS. The Si metasurface embedded in the PDMS is fabricated with an anodized aluminum oxide template followed by Si vapor deposition and sacrificial layer dissolution. Our experimental result reveals that the PDMS containing a metasurface exhibits remarkable electric dipole and magnetic dipole resonances in the visible spectrum. After immersing the metasurface in 20% toluene, the ED and MD resonances shift about 40 nm to red. As a flexible and stretchable elastic membrane, the PDMS containing the large-area metasurface can be easily attached to arbitrarily curved surfaces. Therefore, different from the electron beam lithography (EBL) and focused ion beam (FIB) lithography methods, using our approach not only makes fabricating a metasurface with a large area ($>2\,cm^2$) and dynamic tunability easy but also offers great ease for applications in curved surface devices, such as LEDs, wearable electronics, or other optoelectronic devices.

Acknowledgement

This work was financially supported by the National Natural Science Foundation of China (No. 62075040) and National Key Research and Development Program of China (No. 2021YFF0701100).

References

1. D. Lin, P. Fan, E. Hasman, and M. L. Brongersma, "Dielectric gradient metasurface optical elements," Science **345**, 298 (2014).
2. K. E. Chong, I. Staude, A. James, J. Dominguez, S. Liu, S. Campione, G. S. Subramania, T. S. Luk, M. Decker, D. N. Neshev, I. Brener, and Y. S. Kivshar, "Polarization-independent silicon metadevices for efficient optical wavefront control," Nano Lett. **15**, 5369 (2015).
3. A. Arbabi, Y. Horie, A. J. Ball, M. Bagheri, and A. Faraon, "Subwavelength-thick lenses with high numerical apertures and large efficiency based on high-contrast transmitarrays," Nat. Commun. **6**, 7069 (2015).
4. M. Khorasaninejad, W. T. Chen, R. C. Devlin, J. Oh, A. Y. Zhu, and F. Capasso, "Metalenses at visible wavelengths: diffraction-limited focusing and subwavelength resolution imaging," Science **352**, 1190 (2016).
5. M. Khorasaninejad, A. Y. Zhu, C. Roques-Carmes, W. T. Chen, J. Oh, I. Mishra, R. C. Devlin, and F. Capasso, "Polarization-insensitive metalenses at visible wavelengths," Nano Lett. **16**, 7229 (2016).
6. Z.-P. Zhuang, R. Chen, Z.-B. Fan, X.-N. Pang, and J.-W. Dong, "High focusing efficiency in subdiffraction focusing metalens," Nanophotonics **8**, 1279 (2019).
7. H. Zhou, L. Huang, X. Li, X. Li, G. Geng, K. An, Z. Li, and Y. Wang, "All-dielectric bifocal isotropic metalens for a single-shot hologram generation device," Opt. Express **28**, 21549 (2020).
8. A. I. Kuznetsov, A. E. Miroshnichenko, Y. H. Fu, J. Zhang, and B. Luk'yanchuk, "Magnetic light," Sci. Rep. **2**, 492 (2012).
9. Y. H. Fu, A. I. Kuznetsov, A. E. Miroshnichenko, Y. F. Yu, and B. Luk'yanchuk, "Directional visible light scattering by silicon nanoparticles," Nat. Commun. **4**, 1527 (2013).
10. S. Person, M. Jain, Z. Lapin, J. J. Sáenz, G. Wicks, and L. Novotny, "Demonstration of zero optical backscattering from single nanoparticles," Nano Lett. **13**, 1806 (2013).
11. M. Decker, I. Staude, M. Falkner, J. Dominguez, D. N. Neshev, I. Brener, T. Pertsch, and Y. S. Kivshar, "High-efficiency dielectric Huygens' surface," Adv. Opt. Mater. **3**, 813 (2015).
12. Y. F. Yu, A. Y. Zhu, R. Paniagua-Domínguez, Y. H. Fu, B. Luk'yanchuk, and A. I. Kuznetsov, "High-transmission dielectric metasurface with 2π phase control at visible wavelengths," Laser Photonics Rev. **9**, 412 (2015).
13. Y. Yang, W. Wang, P. Moitra, I. I. Kravchenko, D. P. Briggs, and J. Valentine, "Dielectric meta-reflectarray for broadband linear polarization conversion and optical vortex generation," Nano Lett. **14**, 1394 (2014).
14. A. Arbabi, Y. Horie, M. Bagheri, and A. Faraon, "Dielectric metasurfaces for complete control of phase and polarization with subwavelength spatial resolution and high transmission," Nat. Nanotechnol. **10**, 937 (2015).
15. N. Yu, P. Genevet, M. A. Kats, F. Aieta, J.-P. Tetienne, F. Capasso, and Z. Gaburro, "Light propagation with phase discontinuities: generalized laws of reflection and refraction," Science **334**, 333 (2011).
16. L. Huang, X. Chen, H. Mühlenbernd, H. Zhang, S. Chen, B. Bai, Q. Tan, G. Jin, K.-W. Cheah, C.-W. Qiu, J. Li, T. Zentgraf, and S. Zhang, "Three-dimensional optical holography using a plasmonic metasurface," Nat. Commun. **4**, 2808 (2013).

17. S. Sun, Z. Zhou, C. Zhang, Y. Gao, Z. Duan, S. Xiao, and Q. Song, "All-dielectric full-color printing with TiO_2 metasurfaces," ACS Nano **11**, 4445 (2017).
18. J. Sautter, I. Staude, M. Decker, E. Rusak, D. N. Neshev, I. Brener, and Y. S. Kivshar, "Active tuning of all-dielectric metasurfaces," ACS Nano **9**, 4308 (2015).
19. H.-S. Ee and R. Agarwal, "Tunable metasurface and flat optical zoom lens on a stretchable substrate," Nano Lett. **16**, 2818 (2016).
20. S. M. Kamali, E. Arbabi, A. Arbabi, Y. Horie, and A. Faraon, "Highly tunable elastic dielectric metasurface lenses," Laser Photonics Rev. **10**, 1002 (2016).
21. P. Gutruf, C. Zou, W. Withayachumnankul, M. Bhaskaran, S. Sriram, and C. Fumeaux, "Mechanically tunable dielectric resonator metasurfaces at visible frequencies," ACS Nano **10**, 133 (2016).
22. G. Zhang, C. Lan, H. Bian, R. Gao, and J. Zhou, "Flexible, all-dielectric metasurface fabricated via nanosphere lithography and its applications in sensing," Opt. Express **25**, 22038 (2017).
23. J. Bohn, T. Bucher, K. E. Chong, A. Komar, D.-Y. Choi, D. N. Neshev, Y. S. Kivshar, T. Pertsch, and I. Staude, "Active tuning of spontaneous emission by Mie-resonant dielectric metasurfaces," Nano Lett. **18**, 3461 (2018).
24. A. Komar, R. Paniagua-Domínguez, A. Miroshnichenko, Y. F. Yu, Y. S. Kivshar, A. I. Kuznetsov, and D. Neshev, "Dynamic beam switching by liquid crystal tunable dielectric metasurface," ACS Photonics **5**, 1742 (2018).
25. S. Sun, W. Yang, C. Zhang, J. Jing, Y. Gao, X. Yu, Q. Song, and S. Xiao, "Real-time tunable colors from microfluidic reconfigurable all-dielectric metasurfaces," ACS Nano **12**, 2151 (2018).
26. C. Zhang, J. Jing, Y. Wu, Y. Fan, W. Yang, S. Wang, Q. Song, and S. Xiao, "Stretchable all-dielectric metasurfaces with polarization-insensitive and full-spectrum response," ACS Nano **14**, 1418 (2020).
27. J. Berzinš, S. Indrišiūnas, K. van Erve, A. Nagarajan, S. Fasold, M. Steinert, G. Gerini, P. Gecys, T. Pertsch, S. M. B. Bäumer, and F. Setzpfandt, "Direct and high-throughput fabrication of Mie-resonant metasurfaces via single-pulse laser interference," ACS Nano **14**, 6138 (2020).
28. H. Masuda and K. Fukuda, "Ordered metal nanohole arrays made by a two-step replication of honeycomb structures of anodic alumina," Science **268**, 1466 (1995).
29. H. Masuda, K. Yasui, and K. Nishio, "Fabrication of ordered arrays of multiple nanodots using anodic porous alumina as an evaporation mask," Adv. Mater. **12**, 1031 (2000).
30. I. Staude, A. E. Miroshnichenko, M. Decker, N. T. Fofang, S. Liu, E. Gonzales, J. Dominguez, T. S. Luk, D. N. Neshev, I. Brener, and Y. Kivshar, "Tailoring directional scattering through magnetic and electric resonances in subwavelength silicon nanodisks," ACS Nano **7**, 7824 (2013).
31. G. C. Lisensky, D. J. Campbell, K. J. Beckman, C. E. Calderon, P. W. Doolan, R. M. Ottosen, and A. B. Ellis, "Replication and compression of surface structures with polydimethylsiloxane elastomer," J. Chem. Educ. **76**, 537 (1999).
32. X. Yan, J. Yao, G. Lu, X. Li, J. Zhang, K. Han, and B. Yang, "Fabrication of non-close-packed arrays of colloidal spheres by soft lithography," J. Am. Chem. Soc. **127**, 7688 (2005).
33. J. van de Groep and A. Polman, "Designing dielectric resonators on substrate: combining magnetic and electric resonances," Opt. Express **21**, 26285 (2013).
34. D. Yoo, T. W. Johnson, S. Cherukulappurath, D. J. Norris, and S.-H. Oh, "Template-stripped tunable plasmonic devices on stretchable and rollable substrates," ACS Nano **9**, 10647 (2015).
35. S. M. Kamali, A. Arbabi, E. Arbabi, Y. Horie, and A. Faraon, "Decoupling optical function and geometrical form using conformal flexible dielectric metasurfaces," Nat. Commun. **7**, 11618 (2016).
36. N. Han, L. Huang, and Y. Wang, "Illusion and cloaking using dielectric conformal metasurfaces," Opt. Express **26**, 31625 (2018).
37. Y. Zhou, I. I. Kravchenko, H. Wang, H. Zheng, G. Gu, and J. Valentine, "Multifunctional metaoptics based on bilayer metasurfaces," Light Sci. Appl. **8**, 80 (2019).
38. H. Fudouzi and Y. Xia, "Photonic papers and inks: color writing with colorless materials," Adv. Mater. **15**, 892 (2003).